aerospace

MDPI

Article

Numerical Investigation of the Oblique Detonation Waves and Stability in a Super-Detonative Ram Accelerator

Zhanlin Feng, Kuanliang Wang * and Honghui Teng

School of Aerospace Engineering, Beijing Institute of Technology, Beijing 100081, China; fzl@bit.edu.cn (Z.F.)
* Correspondence: wangkuanliang@bit.edu.cn

Abstract: This study numerically investigates the effects of diluent gas proportion, the overdrive factor, and throat width on the wave structure and thrust performance of a ram accelerator operating in super-detonative mode. For premixed gas of a high energy density, a typical unstart oblique detonation wave system is observed due to the ignition on the front wedge of the projectile, and the detonation waves move downstream to the shoulder as the energy density decreases. In the start range of the overdrive factor, the wave position also shows a tendency to move downstream as the projectile velocity increases, accompanied by oscillations of the wave surface and thrust. As the throat width increases, the wave standing position changes non-monotonously, with an interval of upstream movement and Mach reflection. The typical wave structure of a ram accelerator in super-detonative mode is identified, as well as the unstart stable wave features and the unstable process for choking, which can provide theoretical guidance for avoiding unstart issues in ram accelerators and optimizing their performance.

Keywords: detonation wave; oblique detonation wave; ram accelerator; stability; thrust performance

check for updates

Citation: Feng, Z.; Wang, K.; Teng, H. Numerical Investigation of the Oblique Detonation Waves and Stability in a Super-Detonative Ram Accelerator. *Aerospace* **2023**, *10*, 549. https://doi.org/10.3390/aerospace10060549

Academic Editor: James 'Chris' Thomas

Received: 7 April 2023
Revised: 2 June 2023
Accepted: 6 June 2023
Published: 8 June 2023

1. Introduction

A ram accelerator is a propulsion device that utilizes chemical energy to accelerate a projectile to hypersonic speeds. The projectile enters a tube filled with premixed fuel gas at a supersonic initial velocity, which induces the ignition of the gas by the oblique shock wave (OSW), resulting in the continuous acceleration of the projectile. Theoretically, a ram accelerator can accelerate projectiles to speeds of up to 12 km/s [1]. Since its introduction in 1988 by researchers at the University of Washington [2], the ram accelerator has been studied extensively owing to its exceptional performance and low launch costs [3–5].

Depending on the flow field structure, there are two typical operating modes for a ram accelerator [6,7]: thermal choke mode and super-detonative mode. The thermal choke mode serves as the basic mode for accelerating projectiles to the Chapman–Jouguet (C–J) velocity of the premixed fuel gas, while the super-detonative mode is responsible for further accelerating the projectiles to hypersonic speeds, primarily through the process of oblique detonation combustion, which is crucial for enhancing the projectile's exit velocity. The supersonic combustion of super-detonative mode occurs between the projectile and the tube wall, forming a high-pressure region at the projectile's rear that propels it forward. Furthermore, researchers can modify the thrust performance by adjusting the physico-chemical properties of the premixed fuel gas and the flow path structure (acceleration tube, projectile), among other factors.

Bruckner et al. [8] investigated the influence of premixed fuel gas pressure and reactivity on a ram accelerator and found that the accelerator's acceleration performance improves with increased filling pressure and reactivity of the premixed fuel gas. Kull et al. [9] studied the acceleration mechanism of a ram accelerator by varying the types of premixed fuel gas. The term 'unstart' means that the shock system is pushed ahead of the projectile with the flow choked at its throat, causing the projectile nosecone to be exposed to high pressure, subsonic flow only [10]; this is one of the key challenges faced for ram acceleration. To address the unstart issue in ram accelerators due to heat release, Higgins et al. [11] and Knowlen et al. [12] introduced a baffle-tube ram accelerator by modifying the acceleration tube configuration. The baffle effectively suppressed the forward propagation of the detonation wave, resulting in superior performance compared to conventional smooth-cavity accelerators. Higgins et al. [13–15] also investigated the influence of projectile configuration on the unstart phenomenon and found that modifying the projectile by adding serrations to the tail and base promoted the combustion process, resulting in an unstart result. Additionally, Tomoaki et al. [16] experimentally investigated an improved boat-tail projectile and successfully accelerated it to 1.3 km/s. Teng [17] and Pavalavanni [18] conducted comprehensive research on the shock-induced combustion stability, which provided theoretical analyzing methods for the unstable features of ram accelerators.

These studies primarily focused on the macroscopic performance of super-detonative mode under different control parameters, without addressing the wave structure during the projectile acceleration process. Although these works have analyzed the flow field structure under various parameters, the relationship between the flow field structure and thrust has not been established. Furthermore, a unified characterization of the interplay between different factors is lacking. In fact, due to the typical ram structure of the flow tunnel, the projectile acceleration is closely related to the oblique detonation wave (ODW) [19]. To further explore the flow field wave structure in super-detonative mode, this work comprehensively investigates its variation and evolution by considering factors such as the physicochemical properties of the premixed fuel gas, the projectile overdrive factor (ratio of the projectile velocity to the C–J detonation velocity), and geometric structure. By adjusting the proportion of diluent gas in the premixed fuel gas, the overdrive factor of the projectile, and the throat width of the acceleration tube, we summarize the basic wave characteristics of a ram accelerator operating in the super-detonative mode. The unstable wave motions for a thermally choked unstart were examined, and the variation of ODW structures as well as thrust coefficients in the entire start range were analyzed to clarify the effects of those three factors.

2. Computational Model

2.1. Physical Model

The process of the projectile entering premixed fuel gas at supersonic speeds can be equivalently represented as a supersonic flow passing over a stationary projectile by employing reference frame transformations. In this study, we use the classic projectile configuration shown in Figure 1 [20], and by adjusting the incoming flow parameters and throat width, we simulate the effects of diluent gas proportion n, projectile overdrive factor V, and acceleration tube throat width H on the detonation wave structure within the ram accelerator. The diluent gas proportion, denoted as n, is defined as the ratio of the molecular weight of N_2 in the premixed gases. The projectile overdrive factor is defined as the ratio of the projectile velocity to the C–J detonation velocity. The throat width, denoted as H, signifies the distance from the shoulder of the projectile to the tube wall. The right boundary is set as an outlet with a zero-gradient Neumann boundary condition, which is widely adopted in previous studies on detonation waves [21–23].

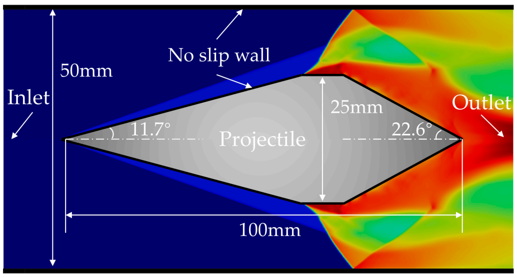

Figure 1. Schematic illustration of calculation model.

In this study, we employ a mixture of hydrogen and oxygen at a stoichiometric equivalence ratio, along with additional nitrogen gas, as the incoming premixed fuel gas. The open-source chemical kinetics software Cantera is used to compute the C–J velocity of the fuel gas [24]. The various parameters used in the case settings are presented in Table 1.

Table 1. Selection of parameters for numerical simulations.

Base Case: 2H_2 + 1O_2 + 5N_2, H = 25, P = 25 atm, T = 300 K									
Nitrogen proportion *n*	3	3.1	3.2	3.3	3.4	3.5	3.6	3.76	5
Overdrive factor V	1.1	1.2	1.3	1.4	1.5	1.6	1.7	-	-
Throat width H (cm)	14	16	18	20	22	24	25	-	-

The value of V for the variables *n* and H is 1.5.

2.2. Governing Equations and Numerical Methods

Uda and Matsuo et al.'s research [25] indicates that the axisymmetric assumption is a reasonable simplification for ram accelerator calculations, as it greatly accelerates the computational speed while preserving the flow field characteristics. Therefore, this study adopts the axisymmetric assumption. Viscosity has also been highlighted as having a significant impact on detonation ignition and wave structure [26], so it is also taken into account in this work. Compared to single-step reaction models, detailed reaction models can more accurately predict chemical reaction processes [27,28]. The accuracy of chemical reactions is crucial for predicting the structure and propagation of the detonation wave [29]. Based on these considerations, the governing equations used in this study are the two-dimensional axisymmetric Navier–Stokes equations with chemical reaction source terms, and the specific form of the equations is as follows:

$$\frac{\partial U}{\partial t}+\frac{\partial E}{\partial x}+\frac{\partial F}{\partial r}+G=\frac{\partial E_v}{\partial x}+\frac{\partial F_v}{\partial r}+G_v+S \tag{1}$$

In the equation, each term can be represented as:

$$U=\begin{bmatrix}\rho\\ \rho u\\ \rho v\\ e_0\\ \rho C_i\end{bmatrix},E=\begin{bmatrix}\rho u\\ p+\rho u^2\\ \rho uv\\ (p+e_0)u\\ \rho uC_i\end{bmatrix},F=\begin{bmatrix}\rho v\\ \rho uv\\ p+\rho v^2\\ (p+e_0)v\\ \rho vC_i\end{bmatrix},G=\frac{1}{r}\begin{bmatrix}\rho v\\ \rho uv\\ \rho v^2\\ (p+e_0)v\\ \rho vC_i\end{bmatrix},S=\begin{bmatrix}0\\ 0\\ 0\\ 0\\ \dot{\omega}_i\end{bmatrix}$$

$$E_v=\begin{bmatrix}0\\ (2\mu+\lambda)\frac{\partial u}{\partial x}+\lambda\frac{\partial v}{\partial r}+\lambda\frac{v}{r}\\ \mu\left(\frac{\partial u}{\partial r}+\frac{\partial v}{\partial x}\right)+\lambda\frac{u}{r}\\ \left[(2\mu+\lambda)\frac{\partial u}{\partial x}+\lambda\frac{\partial v}{\partial r}+\lambda\frac{v}{r}\right]u+\mu\left(\frac{\partial u}{\partial r}+\frac{\partial v}{\partial x}\right)v+\dot{q}_x+\sum_{i=1}^{n_S}\rho D_i h_i\frac{\partial X_i}{\partial x}\\ \rho D_i\frac{\partial X_i}{\partial x}\end{bmatrix},$$

$$F_v=\begin{bmatrix}0\\ \mu\left(\frac{\partial u}{\partial r}+\frac{\partial v}{\partial x}\right)\\ (2\mu+\lambda)\frac{\partial v}{\partial r}+\lambda\frac{\partial u}{\partial x}+\lambda\frac{\partial u}{\partial x}\\ \left[(2\mu+\lambda)\frac{\partial u}{\partial r}+\lambda\frac{\partial v}{\partial x}+\lambda\frac{v}{r}\right]v+\mu\left(\frac{\partial u}{\partial r}+\frac{\partial v}{\partial x}\right)u+\dot{q}_r+\sum_{i=1}^{n_S}\rho D_i h_i\frac{\partial X_i}{\partial r}\\ \rho D_i\frac{\partial X_i}{\partial r}\end{bmatrix},$$

$$G = \frac{1}{r}\begin{bmatrix} 0 \\ \mu\left(\frac{\partial u}{\partial r} + \frac{\partial v}{\partial x}\right) \\ 2\mu\left(\frac{\partial v}{\partial r} + \frac{v}{x}\right) \\ \left[(2\mu+\lambda)\frac{\partial v}{\partial r} + \lambda\frac{\partial u}{\partial x} + \lambda\frac{v}{r}\right]v + \mu\left(\frac{\partial u}{\partial r} + \frac{\partial v}{\partial x}\right)u + \dot{q}_r + \sum_{i=1}^{n_S}\rho D_i h_i \frac{\partial X_i}{\partial r} \\ \rho D_i \frac{\partial X_i}{\partial r} \end{bmatrix}$$

The significance of each dimensionless quantity is as follows: t refers to time, ρ represents the density of the reacting mixture, u and v denote the velocities, C_i represents the mass fraction of the i-th species, x_i denotes the mole fraction of the i-th component and h_i represents the total enthalpy of the i-th component. The pressure p can be calculated using the ideal gas state equation, which is given by:

$$p = \rho RT = \rho T R_u \sum_{i=1}^{n} Y_i W_i \tag{2}$$

where R_u represents the universal gas constant, and W_i denotes the molar mass of the i-th species. The total enthalpy can be calculated as follows:

$$h = \sum_{i=1}^{n} h_i Y_i \tag{3}$$

The stress tensor $\boldsymbol{\tau}$ can be calculated using the following formula:

$$\tau = \mu\left[\nabla u + (\nabla u)^T\right] + \lambda(\nabla \cdot u)I \tag{4}$$

where μ is the dynamic viscosity calculated based on the Sutherland model, and λ denotes the second viscosity, which can be calculated using the following formulas:

$$\mu = \frac{A_s\sqrt{T}}{1 + T_s/T} \tag{5}$$

$$\lambda = -\frac{2}{3}\mu \tag{6}$$

The Sutherland coefficients are given by A_s = 1.458 × 10^{-6}, T_s = 111.

In the governing equations, the chemical reaction rate is calculated using the Arrhenius formula, where J_i is the mass diffusion flux, which can be expressed as:

$$J_i = \rho D_i \nabla Y_i \tag{7}$$

where D_i represents the diffusion coefficient, and its calculation model is as follows:

$$\rho D_i = \frac{\mu}{S_{ti}} \tag{8}$$

The Schmidt number, S_{ti}, is treated as a constant in this calculation.

In this study, Jachimowski's hydrogen combustion mechanism is employed to simulate the chemical reactions [30], which involve nineteen reversible elementary reactions among nine components. This detailed chemical reaction mechanism has been successfully applied in previous detonation simulations [31,32]. The computational program is based on the finite volume method, with a second-order conservative TVD scheme [33]. The HLLC (Harten–Lax–van Leer Contact) approximate Riemann solver is employed for the calculation of interface fluxes [34]. In the time direction, an explicit fourth-order Runge–Kutta method is adopted.

2.3. Mesh Refinement Verification

Choosing an appropriate grid resolution is crucial for the accuracy of numerical simulations. When simulating detonation waves, the thickness of the wavefront is only on the order of micrometers [35], necessitating the use of high-resolution grids for accurate simulations.

To ensure that the computational results are not influenced by the spatial discretization scale, the base case was calculated using grid sizes of 100 µm and 200 µm. Figure 2 shows a comparison of the flow fields for the 100 µm and 200 µm grids, indicating that both grid resolutions can accurately simulate the shock waves and detonation waves in the flow field. By extracting the pressure and temperature distributions near the wall of the accelerator tube, as shown in Figure 3, it can be seen that the values and trends for both variables are nearly identical for the different grid sizes. The 200 µm grid is sufficient to capture the fine features of the flow field and ensure that the numerical results are not influenced by the grid size. Therefore, the results presented in this paper are based on numerical calculations with a 200 µm grid.

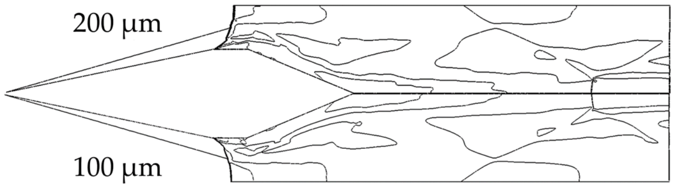

Figure 2. Temperature fields with different grid scales.

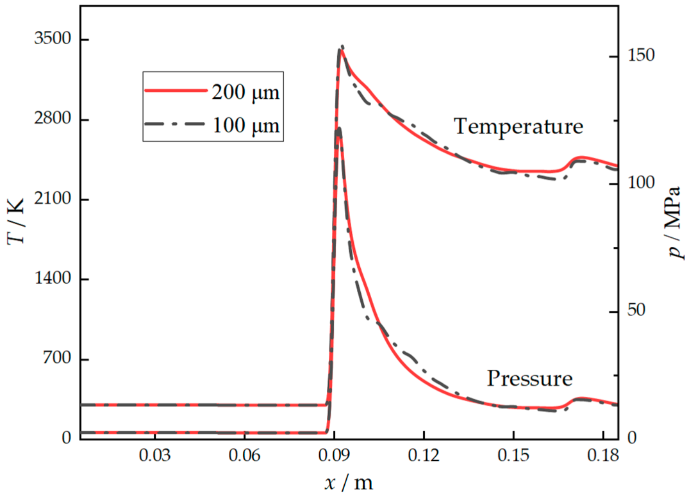

Figure 3. Distribution of pressure and temperature along the wall with different grid sizes.

3. Results and Discussion

3.1. Influence of Dilution Gas Proportion on Ram Accelerator Performance

The energy content of premixed gas can affect the speed and strength of the detonation wave [36], and in this study, the energy density is modified by adding different proportions of N_2 to the premixed gas. The advantage of using N_2 lies in its stability in H_2/Air combustion, where it rarely acts as a reactant and does not introduce an additional component. Therefore, the composition of the premixed gas in this study was set as $2H_2 + 1O_2 + nN_2$, with n ranging from 3 to 5.

Figure 4 shows the pressure fields within the ram accelerator at $n = 3$, where a typical unstart wave system is formed after the detonation region has fully developed. At the front of the flow field, the premixed gas undergoes a chemical reaction on the projectile's leading wedge surface, resulting in the formation of a detonation wave [37]. Subsequently, the established detonation wave experiences two successive regular reflections on the upper wall and the projectile's leading wedge surface, leading to an elevation in pressure of the detonation products and an amplification of negative thrust. At the rear of the flow field, the flow near the projectile is suddenly deflected outward due to the geometric structure, forming an expansion wave, and since the isentropic expansion occurs at the aft wedge surface, a low-pressure zone is formed instead of a recirculation zone. The shock wave from the second reflection undergoes a third reflection on the tube wall and is deflected inward due to the influence of the low-pressure zone, to some extent mitigating the deterioration of ram accelerator performance.

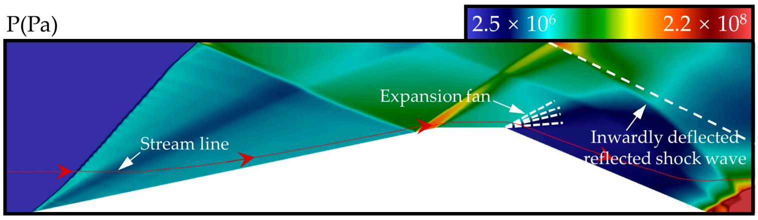

Figure 4. Pressure fields, streamlines (red curves) and expansion fan (white dotted line) at $n = 3$.

Figure 5 shows the flow field structure within the ram accelerator at $n = 3.1$. Compared to the case with $n = 3$, flow separation occurs after the flow passes the projectile's shoulder and a separation zone is formed at the aft wedge surface. Due to the expansion of the separation zone, a separation bubble that crosses the projectile's shoulder is generated, disturbing the incoming flow and creating a compression wave behind the projectile's shoulder. To accommodate the changes in the thermodynamic and flow states downstream of the compression wave, the angles of the upstream detonation wave and the second reflected shock wave both increase from 41° to 44°. Although increasing the dilution gas ratio reduces the energy density of the premixed gas, which suppresses the upstream propagation of the detonation wave, the change in flow state caused by the recirculation zone has a greater impact on the upstream flow. Therefore, when n changes from 3 to 3.1, the thrust performance further deteriorates, and the ram accelerator remains in an unstart state.

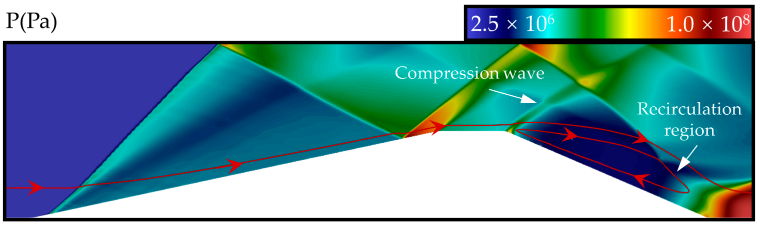

Figure 5. Pressure fields and streamlines (red curves) at $n = 3.1$.

Figure 6 shows the flow field structure within the ram accelerator at $n = 3.2$. In this case, the structure of the detonation wave transforms into a standard abrupt structure, and the ignition position of the detonation wave shifts downstream. After reflecting off the wall, the detonation wave intersects with the compression wave, and the reflected shock wave directly crosses the projectile's shoulder, constraining the position of the recirculation zone. This containment compresses the product in the area, increasing the average pressure at the aft wedge surface of the projectile, and the ram accelerator starts to generate positive thrust.

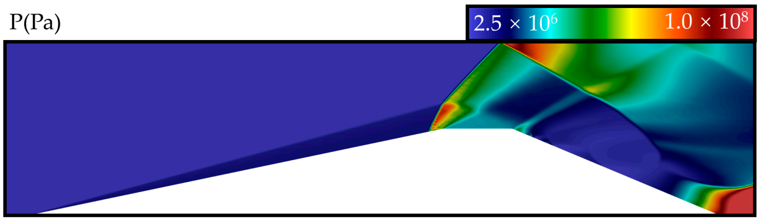

Figure 6. Pressure fields at $n = 3.2$.

Figure 7 shows the flow field structure inside the ram accelerator at $n = 3.3$ and 3.4. The upper figure presents the results for $n = 3.3$; as the energy density of the premixed gas further decreases, the ignition position of the detonation wave moves downstream to the head of the projectile's shoulder. A normal detonation wave (NDW) is formed from the projectile's shoulder by the expansion wave, and the NDW–ODW transition structure can be seen. In this condition, the detonation wave no longer generates a negative thrust on the projectile's front wedge surface, causing the projectile's thrust to increase. The lower figure shows the results for $n = 3.4$; influenced by the expansion wave at the front end of the projectile's shoulder, the detonation wave after the OSW remains in a weakly driven state. As the proportion of diluent gas in the premixed gas increases, the heat release of combustion decreases, leading to a decline in the driving capability. The detonation wave after the OSW transitions from the NDW to the ODW. When $n = 3.5$ and $n = 3.6$, the changing trend of the flow field structure is similar to the aforementioned cases, and the thrust continues to decline.

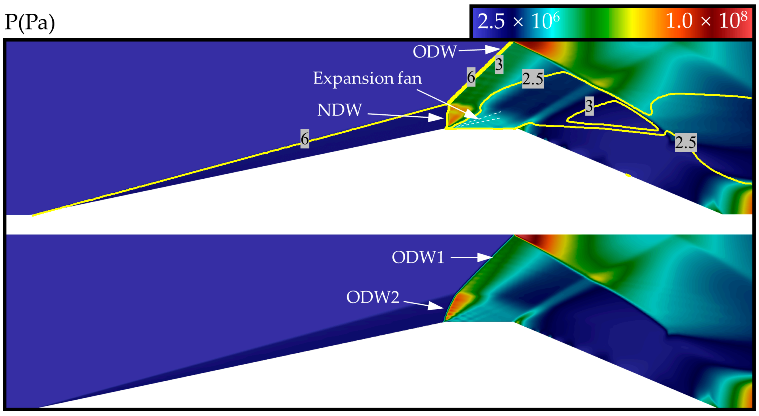

Figure 7. Pressure fields and Mach number contour lines (yellow lines) at $n = 3.3$ (**upper**) and $n = 3.4$ (**lower**).

Ram accelerators have many similarities with ramjet engines in principle, and studying ram accelerators can provide valuable guidance for the design of ramjet engines. As a typical air-breathing engine, the ramjet engine does not require an onboard oxidizer during operation; it can capture the oxidizer from the air through the intake. Since the composition of air is $1O_2 + 3.76N_2$, it is of great significance to study the flow field structure of a ram accelerator at $n = 3.76$ separately. Figure 8 shows the flow field structure inside the ram accelerator at $n = 3.76$, at which point the ignition position of the detonation wave moves further downstream, and the expansion wave behind the detonation wave disappears, replaced by the gaseous wedge surface generated by the upstream propagation of the recirculation zone. The function of this gaseous wedge is similar to that of a heated physical wedge: on the one hand, it provides part of the heat required for the reaction, and on the other hand, it prevents the detonation wave front from moving downstream. Figure 8 shows the local streamline diagram of the gaseous wedge and recirculation zone, where a total of three streamwise vortex structures are generated from the upstream to downstream flow field. Vortex 3 is a typical separation vortex, and the fluid inside the projectile's boundary layer forms vortex 2 under the combined action of viscous force and the back pressure of vortex 3. Vortex 2 changes the flow inside the gaseous wedge and forms vortex 1. The interaction of the three vortices allows the gaseous wedge to stably exist, so the oblique detonation wave can also stably reside at the projectile's shoulder. As for the thrust, due to the decrease in energy density of the premixed gas, the thrust performance also declines.

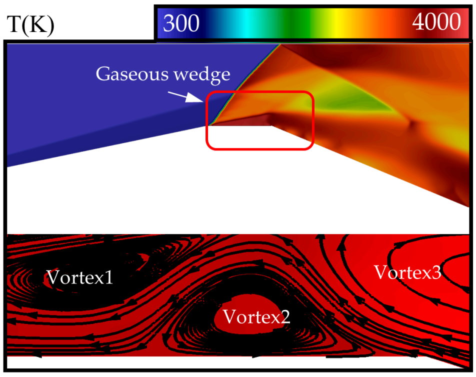

Figure 8. Temperature fields (**upper**) and gaseous wedge local structures (**lower**) at n = 3.76.

Figure 9 illustrates the flow field structure inside the ram accelerator at n = 5, which is similar to that at n = 3.76. As the heat release from the reaction decreases, the thrust generated by the expansion of the detonation products is gradually counteracted by the shock wave resistance on the forward wedge surface, resulting in a further deterioration of the thrust performance.

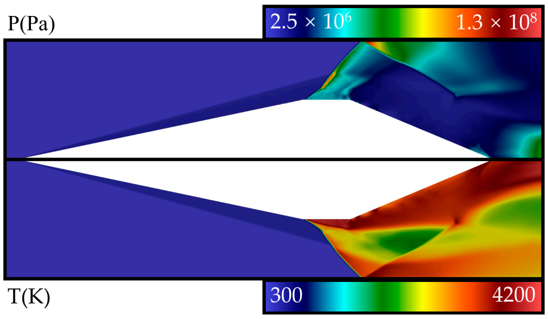

Figure 9. Pressure fields (**upper**) and temperature fields (**lower**) at n = 5.

The thrust coefficient, which is defined as the ratio of the thrust acting on the body and the initial pressure on the projectile cross section, was calculated for each operating condition, and the variation trends are illustrated in Figure 10. It can be observed that the thrust performance is optimal at n = 3.4. When n is less than 3.2, the ram accelerator enters the unstarting state. When n is greater than or equal to 3.2, the ram accelerator can generate positive thrust. Moreover, it can be anticipated that when n becomes too large, the shock wave resistance exceeds the positive thrust, leading to acceleration failure in the ram accelerator.

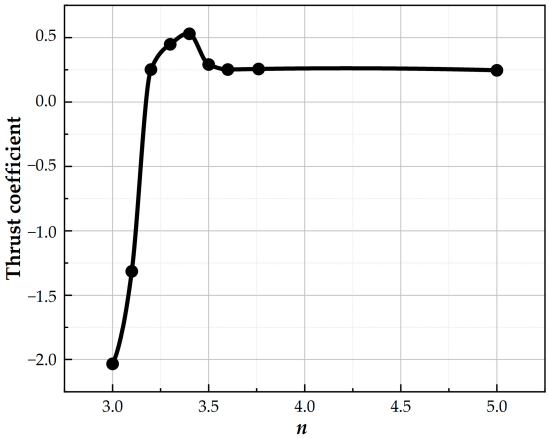

Figure 10. Thrust coefficients for various values of n.

3.2. Flow Field Structures and Performance under Different Overdrive Factors

When the super-detonative ram accelerator operates, the projectile is subjected to a continuous thrust and accelerates. The velocity of the projectile corresponds to different wave structures, which in turn determine the magnitude of the thrust on the projectile. Typically, operation of the ram accelerator is initiated in the thermally choked mode at low velocities, and the transition to other modes occurs at velocities near the C–J detonation speed of the gas mixture. Furthermore, many studies use a certain range in excess of the C–J detonation speed to define several modes of ram accelerator operation [38] and refer to the ratio of the projectile velocity to the C–J velocity of the premixed gas as the "overdrive factor". Thus, we continue to use the overdrive factor as a variable and analyze the flow fields in the range of 1.1 to 1.7, denoted as V.

When the overdrive factor V is 1.1, the detonation wave experiences a choking unstart instability, as shown in Figure 11. Figure 11 depicts the flow field structure of the shock accelerator at t = 140 μs, along with the temperature and pressure distribution. The yellow solid line is the contour line of Mach number 1, revealing that the detonation wave is divided into an ODW within the OSW, and a NDW outside the OSW. The flow behind the ODW within the OSW is supersonic, while the flow behind the NDW outside the OSW is subsonic, which is an overdriven normal detonation wave. The overdriven normal detonation wave moves upstream, driving the ODW, which gradually contracts during this process. By comparing the detonation wave fronts at different moments, it can be observed that this upstream development process is an accelerated one, which also leads to a rapid increase in the negative thrust.

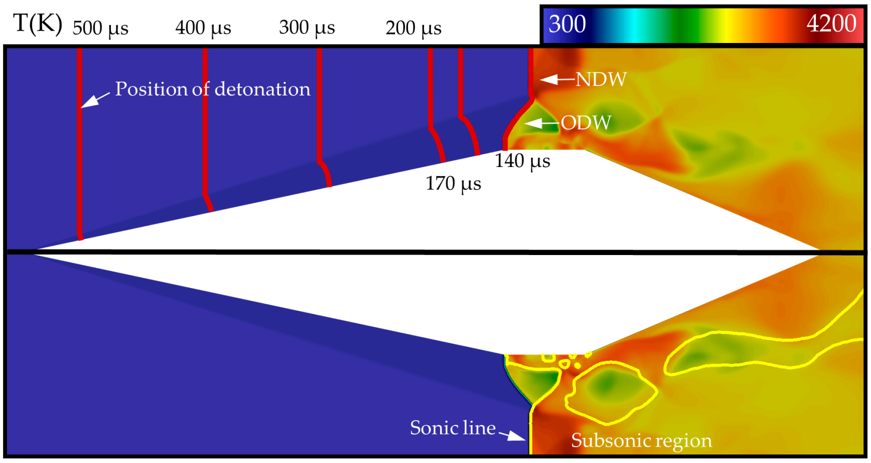

Figure 11. Temporal evolution of detonation and sonic line positions (yellow lines) at t = 140 μs when V = 1.1.

When the overdrive factor V is 1.2, the detonation wave oscillates at the front end of the projectile shoulder; Figure 12 shows the waveforms of the wavefront oscillating to the farthest upstream and downstream positions. Under this condition, the detonation wave cannot propagate upstream and is in a critical stable state, whose wave structure is similar to the initial state of 1.1. The region above the triple-point essentially maintains an NDW, but the reaction front below the triple-point changes constantly at the leading edge of the shoulder. The formation of this oscillation phenomenon is related to the interaction of shock–wall–heat release, and although the cause is difficult to determine, it can be seen that the heat released by the reaction below is no longer enough to maintain the wavefront at 1.1. Furthermore, by calculating the thrust performance, we find that the fluctuation of thrust is the largest in either state.

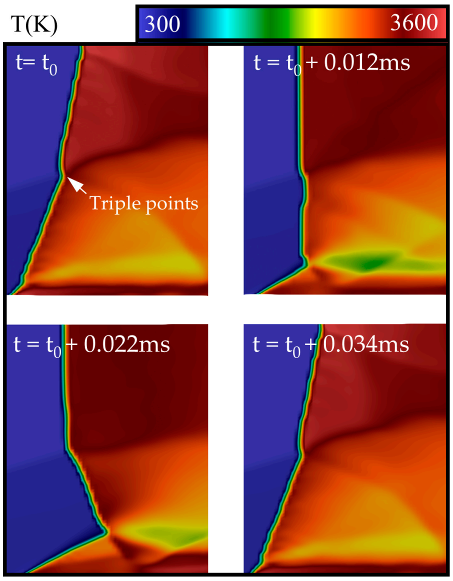

Figure 12. Periodic detonation wave structures at V = 1.2.

Figure 13 depicts the flow field structures for overdrive factors V ranging from 1.3 to 1.6, showing that the detonation wave angle gradually decreases as the projectile speed increases. Figure 13a presents the pressure distribution at a V value of 1.3, where the detonation wave angle is still greater than the critical angle for shock wave reflection, forming Mach reflection on the upper wall. The restrictive effect of the reflected shock wave on the recirculation zone further increases the positive thrust on projectile. The positive thrust at V = 1.2 is about 11,294 N, and the positive thrust at V = 1.3 is about 17,942 N. Meanwhile, the shock wave resistance increased from 7854 N to 10,453 N. This suggests that the decrease in the overall thrust coefficient was caused by the increase in shock wave resistance. At a V value of 1.4, the detonation wave angle becomes less than the critical angle for shock wave reflection, and the reflected shock wave on the upper wall changes to a regular reflection. As the reflection point moves rearward, the restrictive effect of the reflected shock wave on the recirculation zone weakens, while the shock wave resistance increases, leading to a decline in the performance of the ram accelerator. The flow field structures and thrust changes follow the same trend for V values of 1.5 and 1.6, and the detonation wave front in the V range of 1.3 to 1.6 also oscillates.

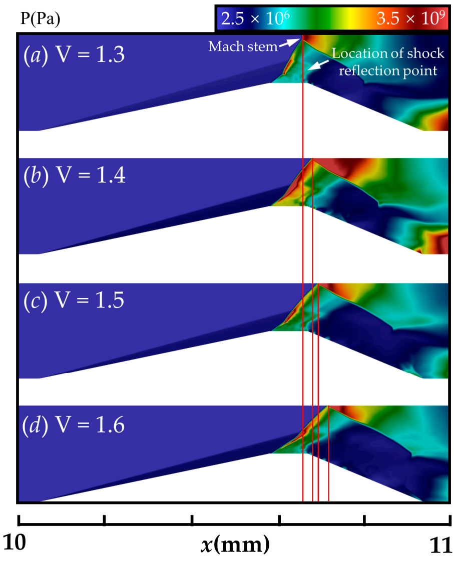

Figure 13. Flow field structures at overdrive factors of (**a**) 1.3, (**b**) 1.4, (**c**) 1.5 and (**d**) 1.6.

Figure 14 shows the flow field structure when the overdrive factor is 1.7. As the overdrive factor increases, disturbances of the recirculation zone no longer affect the macroscopic structure of the detonation wave, which becomes a stable ODW on the projectile shoulder. The thrust no longer oscillates due to the almost unchanged ODW structure; nevertheless, its performance is approaching failure for this condition because of the increased inflow resistance. The dimensionless thrust coefficients were calculated under different operating conditions, and the results are shown in Figure 15. When V = 1.3, the performance of the ram accelerator reaches its optimum, and deviating from this condition will cause the ram accelerator's performance to decline or even fail due to the combined effects of inflow shock wave resistance and changes in the detonation wave system; furthermore, if the stability of thrust is considered, the optimal performance point may not be the most stable point.

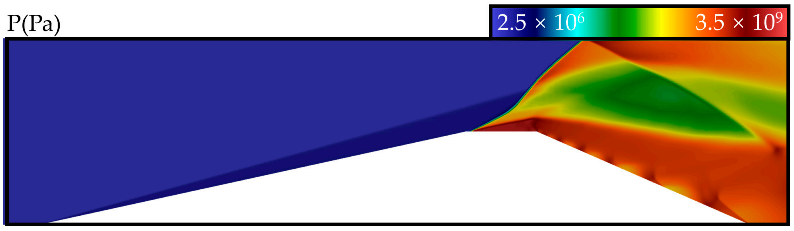

Figure 14. Flow field structure at a V value of 1.7.

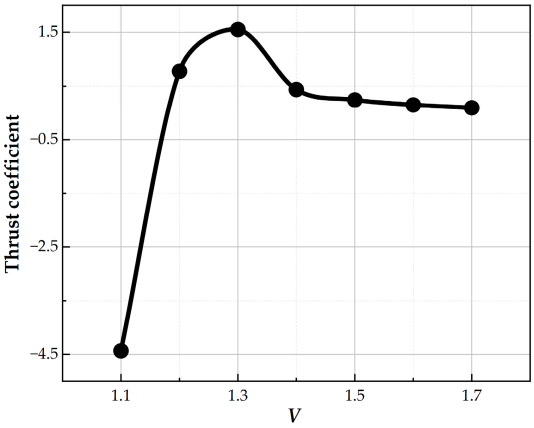

Figure 15. Thrust coefficients for various values of V.

3.3. Influence of Throat Width on Ram Accelerator Performance

Previous research [39] has pointed out that the contraction ratio within the intake duct is one of the key factors causing the unstart problem. Due to the similarities in working principles between the scramjet engine and the ram accelerator, it is of great significance to study the influence of throat width H on the ram accelerator. In this study, the throat width H was used as a variable, ranging from H = 14 to 25, and the flow field characteristics from thermal choking to stable operations under different contraction ratios were compared.

As shown in Figure 16 by the wavefront positions at different times, a typical thermal choking instability process occurs for H = 14. Under this condition, both of the detonation waves, inside and outside the oblique shock wave, are overdriven detonation waves, and this unstable detonation wave will gradually propagate upstream, leading to the failure of the ram accelerator. Unlike the instability process shown in Figure 11, the detonation wave within the oblique shock wave in this condition spontaneously propagates upstream due to the excessive overdrive degree, which makes the performance of the ram accelerator decline more rapidly.

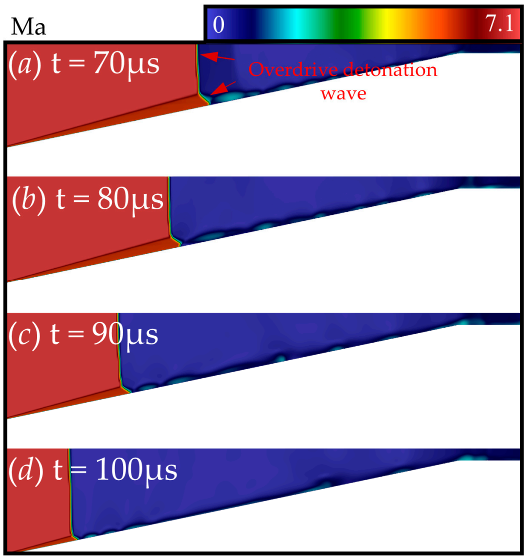

Figure 16. Choking instability process of detonation at H = 14: (**a**) t = 70 μs, (**b**) t = 80 μs, (**c**) t = 90 μs and (**d**) t = 100 μs.

As shown in Figure 17, when H = 16, the ODW front stops at the throat entrance and undergoes regular reflection on the upper wall. The inflow experiences a sudden pressure increase after the reflected shock wave, and an adverse pressure gradient forms in the boundary layer upstream of the reflected shock wave, leading to boundary layer separation and the formation of a separation bubble, as shown in the figure. The reflected shock wave undergoes a second reflection behind the separation bubble, and the inflow near the projectile wall experiences a Prandtl–Meyer expansion after passing through the second reflected shock wave at the rear wedge surface of the projectile, thus avoiding the formation of a recirculation zone. At this width, the thrust generated by the detonation combustion is all positive, allowing the ram accelerator to operate normally. However, due to the gradual weakening of the shock wave's strength after multiple reflections, its restrictive effect on the gas expanding at the projectile's rear wedge surface is very weak, resulting in a relatively weak performance of the ram accelerator.

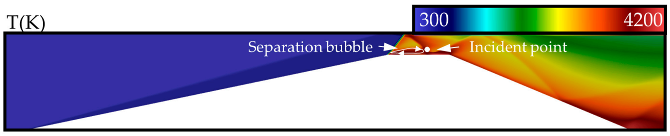

Figure 17. Temperature field at H = 16.

When H is increased to 18, the detonation wavefront position shifts downstream; the resultant flow field structure is shown in Figure 18. In this case, a three-streamwise vortex structure, similar to that shown in Figure 8, is formed near the projectile shoulder, with the gaseous wedge created by the three vortices maintaining the stability of the detonation wavefront. Due to the downstream shift of the detonation wave's position, the location of the reflected shock wave also shifts downstream, enhancing its restrictive effect on the recirculation zone and improving the performance of the ram accelerator.

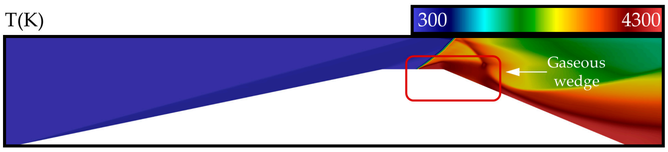

Figure 18. Temperature field at H = 18.

Figure 19 shows the flow field structures when H is increased to 20 and 22, respectively. The flow field structure for when H is increased to 20 is shown in Figure 19. As the throat width increases, the detonation products expand sufficiently downstream, and the ODW surface moves upstream. The ODW angle becomes larger than the critical angle for shock wave reflection, leading to a Mach reflection on the upper wall. The reflected shock wave formed by the Mach reflection has a greater intensity than that formed by the regular reflection, resulting in the optimal thrust performance of the ram accelerator. The flow field structure for when H is increased to 22 is shown in Figure 19. The detonation products overexpand at the projectile's rear wedge surface, causing the detonation wave angle to decrease and become smaller than the critical angle for shock wave reflection again. The Mach reflection on the upper wall changes to a regular reflection, and the thrust performance declines accordingly. When H is increased to 25, the thrust performance decreases further, and the flow field structure becomes the standard super-detonative ram accelerator flow field structure, such as the one shown in Figure 9.

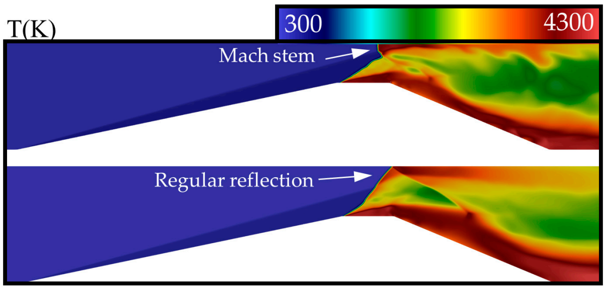

Figure 19. Temperature field at H = 20 (**upper**) and H = 22 (**lower**).

The dimensionless thrust coefficients were calculated for each throat width, and their magnitudes and variations are illustrated in Figure 20. The ram accelerator performance reaches its optimum when H = 20. When the throat width is too small, the ram accelerator may enter an unstart state due to thermal choking. When the throat width is too large, the detonation products overexpand at the projectile's rear wedge surface, leading to a decline in the ram accelerator's thrust performance.

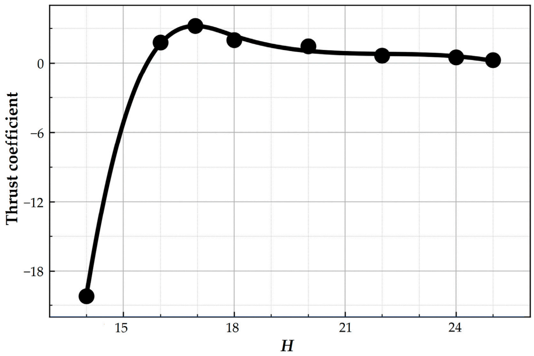

Figure 20. Thrust coefficients for various values of H.

The present study is an attempt to understand the unified characteristics of wave systems in a detonation-driven accelerator. Through the analysis of the flow field under various variables, it can be found that the super-detonative mode accelerator has a similar structure, as shown in Figure 21. The projectile's leading wedge surface induces an ODW, which compresses the premixed fuel to improve combustion efficiency. Under the combined action of the boundary layer at the projectile's shoulder and the sudden expansion of the trailing wedge surface, a three-flow-direction vortex forms a gaseous wedge surface and recirculation zone, allowing the detonation wave to be stationary at the projectile's shoulder, generating positive thrust. Furthermore, for the choking unstart instability phenomenon, the motion process can be distinguished into a weak detonation and a strong detonation by the sonic line.

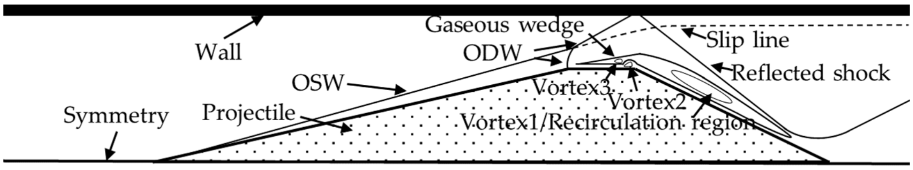

Figure 21. Typical flow field structures of a ram accelerator in super-detonative mode.

4. Conclusions

In this study, the finite volume method was used to solve the two-dimensional axisymmetric Navier–Stokes equations with chemical reaction source terms. Numerical simulations were conducted to investigate the effects of the gas dilution ratio, overdrive factor, and throat width on the performance of ram accelerators. The following conclusions were drawn:

(1) For each factor affecting the ram accelerator, there exists a unique design point that maximizes its thrust performance. Once the thrust performance of the ram accelerator begins to deteriorate, this deterioration trend is irreversible. Therefore, identifying the design points for each parameter is essential for optimizing the thrust performance of ram accelerators.
(2) The detonation wave structure within the ram accelerator is highly sensitive to the heat release of reaction species. Furthermore, the choking of the flow field can be caused by excessive heat release or restricted heat transport downstream.
(3) Regardless of the design parameter adjustments, when the ram accelerator operates stably in the super-detonative mode, it exhibits the same wave structure. The formation of the gaseous wedge is crucial for ensuring the normal operation of the ram accelerator.
(4) As the projectile accelerates, wave oscillations near its shoulder occur, and these oscillations are weakened by projectile movements with high overdrive factors and also by reducing the heat release of the reaction.

Author Contributions: Conceptualization, formal analysis, investigation, data curation, writing—original draft, Z.F.; methodology, writing—review and editing, visualization, K.W.; supervision, project administration, funding acquisition, H.T. All authors have read and agreed to the published version of the manuscript.

Funding: This research was supported by the National Natural Science Foundation of China (NSFC) (No. 12002041).

Data Availability Statement: Data are contained within the article.

Conflicts of Interest: The authors declare no conflict of interest.

References

1. Wenzel, A.B. A Review of explosive accelerators for hypervelocity impact. *Int. J. Impact. Eng.* **1987**, *5*, 682–693. [CrossRef]
2. Hertzberg, A.; Bruckner, A.P.; Bogdanoff, D.W. Ram accelerator: A new chemical method for accelerating projectiles to ultrahigh velocities. *AIAA J.* **1988**, *26*, 195–203. [CrossRef]
3. Zhou, R.X.; Meng, F.Z.; Li, T.; Li, Z.P.; Lian, H. Ram to scram mode transition in a simulation flight acceleration. *Phys. Fluids* **2022**, *34*, 066114. [CrossRef]
4. Yang, Z.Z.; Zhang, B. Numerical and experimental analysis of detonation induced by shock wave focusing. *Combust. Flame* **2023**, *251*, 112691. [CrossRef]
5. Qin, Q.Y.; Zhang, X.B. Controllable initiation characteristics of the oblique detonation wave in a combustor with a confined cone of a novel structure. *Aerosp. Sci. Technol.* **2020**, *107*, 106267. [CrossRef]
6. Li, C.; Kailasanath, K.; Oran, E.S. Detonation structures generated by multiple shocks on ram-accelerator projectiles. *Combust. Flame* **1997**, *108*, 173–186. [CrossRef]

7. Nettleton, M.A. The applications of unsteady, multi-dimensional studies of detonation waves to ram accelerators. *Shock Wave* **2000**, *10*, 9–22. [CrossRef]
8. Bruckner, A.P.; Bogdanoff, D.W.; Knowlen, C. Investigation of gas-dynamic phenomena associated with the ram accelerator concept. In Proceedings of the AIAA 19th Fluid Dynamic, Plasma Dynamic and Lasers Conference, Honolulu, HI, USA, 8–10 June 1987.
9. Kull, A.E.; Bumham, E.A.; Knowlen, C. Experimental studies of super-detonative ram accelerator modes. In Proceedings of the AIAA/ASME/SAE/ASEE 25th Joint Propulsion Conference, Monterey, CA, USA, 10–13 July 1989.
10. Liu, S.Z. Axis-Symmetric Ram Accelerator Projectile Performance Characteristics. Master's Thesis, University of Washington, Seattle, WA, USA, 2019.
11. Higgins, A.J. Ram accelerators: Outstanding issues and new directions. *J. Prop. Power* **2006**, *22*, 1170–1187. [CrossRef]
12. Knowlen, C.; Glusman, J.; Grist, R. Experimental investigation of a baffled-tube ram accelerator. In Proceedings of the 52nd AIAA/SAE/ASEE Joint Propulsion Conference, Salt Lake City, UT, USA, 25–27 July 2016.
13. Knowlen, C.; Leege, B.J.; Daneshvaran, N. Ram accelerator operation in railed and baffled tubes. In Proceedings of the AIAA Propulsion and Energy 2020 Forum, Online, 24–28 August 2020.
14. Daneshvaran, N.; Leege, B.J.; Knowlen, C. Computational fluid dynamic modeling of railed tube ram accelerator in reactive flow. In Proceedings of the AIAA SCITECH 2022 Forum, San Diego, CA, USA, 3–7 January 2022.
15. Leege, B.J.; Simth, C.; Knowlen, C. Baffled tube ram accelerator operation with normal baffles. In Proceedings of the AIAA SCITECH 2022 Forum, San Diego, CA, USA, 3–7 January 2022.
16. Tomoaki, Y.; Chang, X.Y.; Taki, K. Experiments on flame holding position of the fin-less projectile in ram accelerator. In Proceedings of the 10th AIAA/NAL-NASDA-ISAS International Space Planes and Hypersonic Systems and Technologies Conference, Kyoto, Japan, 24–27 April 2001.
17. Jiang, Z.L.; Teng, H.H. *Gaseous Detonation Physics and Its Universal Framework Theory*, 1st ed.; Springer: Singapore, 2022; pp. 187–227.
18. Pavalavanni, P.K.; Jo, M.S.; Kim, J.E. Numerical study of unstable shock-induced combustion with different chemical kinetics and investigation of the instability using modal decomposition technique. *Aerospace* **2023**, *10*, 292. [CrossRef]
19. Choi, J.Y.; Jeung, I.S. *Numerical Simulation of Super-Detonation Ram Accelerator*; Its Shock-Induced Combustion and Oblique Detonation; Springer Nature Switzerland AG: Cham, Switzerland, 2016; pp. 217–267.
20. Choi, J.Y.; Lee, B.J.; Jenug, I.S. Computational modeling of high-pressure combustion mechanism in scram accelerator. *J. Phys. IV* **2000**, *11*, 131–141. [CrossRef]
21. Zhang, Y.; Fang, Y.; Ng, H.D.; Teng, H.H. Numerical investigation on the initiation of oblique detonation waves in stoichiometric acetylene–oxygen mixtures with high argon dilution. *Combust. Flame* **2019**, *204*, 391–396. [CrossRef]
22. Yang, P.F.; Ng, H.D.; Teng, H.H. Numerical study of wedge-induced oblique detonations in unsteady flow. *J. Fluid Mech.* **2019**, *876*, 264–287. [CrossRef]
23. Wang, K.L.; Yang, P.F.; Teng, H.H. Steadiness of wave complex induced by oblique detonation wave reflection before an expansion corner. *Aerosp. Sci. Technol.* **2021**, *112*, 106592. [CrossRef]
24. Gorbatenko, I.; Bradley, D.; Tomlin, A.S. Auto-ignition and detonation of n-butanol and toluene reference fuel blends (TRF). *Combust. Flame* **2019**, *229*, 111378. [CrossRef]
25. Uda, Y.; Matsuo, A. Three-dimensional numerical simulation of shock-induced combustion around a blunt body. In Proceedings of the 21st International Colloquium on the Dynamics of Explosions and Reactive Systems, Poitiers, France, 23–27 July 2007.
26. Teng, H.H.; Liu, S.; Zhang, Z.J. Unsteady combustion mode with a super-high frequency induced by a curved shock. *Phys. Fluids* **2020**, *32*, 116101. [CrossRef]
27. Dangerfield, T.L.; Paik, I.; Bhadra, S.; Johnson, K.A. Kinetics of elementary steps in loop-mediated isothermal amplification (LAMP) show that strand invasion during initiation is rate-limiting. *Nucleic Acids Res.* **2022**, *51*, 488–499. [CrossRef] [PubMed]
28. Xiang, G.X.; Zhang, Y.C.; Gao, X. Oblique detonation waves induced by two symmetrical wedges in hydrogen-air mixtures. *Fuel* **2021**, *295*, 120615. [CrossRef]
29. Dai, J.; Peng, L.Y. Numerical investigation on detonation initiation and propagation with a symmetric-jet in supersonic combustible gas. *Aerospace* **2022**, *9*, 501. [CrossRef]
30. NASA Technical Reports Server. Available online: https://ntrs.nasa.gov/citations/19880006464 (accessed on 7 March 2023).
31. Choi, J.Y.; Shin, J.R.; Jeung, I.S. Unstable combustion induced by oblique shock waves at the non-attaching condition of the oblique detonation wave. *Proc. Combust. Inst.* **2009**, *32*, 2387–2396. [CrossRef]
32. Zhang, L.; Sheng, Z.Q.; Dan, Y. Effects of sawtooth grooves on supersonic combustion. *Aerosp. Sci. Technol.* **2023**, *136*, 108223. [CrossRef]
33. Peroomian, O.; Chakravarthy, S.; Goldberg, U. A 'grid-Transparent' methodology for CFD. In Proceedings of the 35th Aerospace Sciences Meeting and Exhibit, Reno, NV, USA, 6–9 January 1997.
34. Toro, E.F.; Spruce, M.; Speares, W. Restoration of the contact surface in the HLL-Riemann solver. *Shock Waves* **1994**, *4*, 25–34. [CrossRef]
35. Teng, H.H.; Bian, J.; Zhou, L.; Zhang, Y.N. A numerical investigation of oblique detonation waves in hydrogen-air mixtures at low mach numbers. *Int. J. Hydrogen Energy* **2021**, *46*, 984–994. [CrossRef]
36. Lee, J. Dynamic parameters of gaseous detonations. *Annu. Rev. Fluid Mech.* **1984**, *16*, 311–336. [CrossRef]

37. Bachman, C.L.; Goodwin, G.B. Ignition criteria and the effect of boundary layers on wedge-stabilized oblique detonation waves. *Combust. Flame* **2021**, *223*, 271–283. [CrossRef]
38. Choi, J.Y.; Jenug, I.S.; Yoon, Y. Numerical study of scram aerator starting characteristics. *AIAA J.* **2013**, *36*, 1029–1038. [CrossRef]
39. Yu, K.K.; Xu, J.L.; Liu, S.; Zhang, X.F. Starting characteristics and phenomenon of a supersonic wind tunnel coupled with inlet model. *Aerosp. Sci. Technol.* **2018**, *77*, 626–637. [CrossRef]